Acta Cryst. (1997). A53, 242–250

The Electrostatic Contribution to the Forward-Scattering Potential at a Space Charge Layer in High-Energy Electron Diffraction. II. Fringing Fields

R. E. DUNIN-BORKOWSKI* AND W. O. SAXTON

Department of Materials Science and Metallurgy, Pembroke Street, Cambridge CB2 3QZ, England. E-mail: red10@cam.ac.uk

(Received 29 August 1996; accepted 9 December 1996)

Abstract

The electrostatic potential is determined both inside and outside a parallel-sided dielectric slab that contains a space charge layer whose plane is perpendicular to the surfaces of the slab, with particular reference to the use of phase-contrast techniques in transmission electron microscopy to characterize such layers.

1. Introduction

An interfacial space charge layer in a dielectric, such as that at a doped grain boundary in a ceramic, typically comprises a sheet of charged impurities or defects surrounded by a broader distribution of oppositely charged free carriers. In paper I (Dunin-Borkowski, Saxton & Stobbs, 1996), we determined the form of the electrostatic potential at such a layer with the aim of relating phase contrast visible at the layer in the transmission electron microscope (TEM) to the form of the free carrier charge distribution. However, our calculations did not take into account the fact that a TEM foil has a finite thickness (usually less than 1 μm). Accordingly, here we use classical image charge theory to assess the effect of finite specimen thickness on the potential both inside and outside a parallel-sided dielectric slab, which contains a space charge layer whose plane is perpendicular to the specimen surfaces,† illustrating our results for a material that has representative values for both the width and the charge density at a space charge layer. In the present work, we assume that the relative permittivity within the slab is constant across the space charge layer and that classical image charge interactions are valid on a scale of a few atomic diameters. The latter assumption strictly requires the electric field to vary slowly over atomic dimensions (*e.g.* Finnis, 1991) and so it should be noted that, in the limit of the narrowest charge distributions and the thinnest specimens, the calculations presented here may not be quantitatively accurate. Similar calculations have been presented for both reverse-biased *p–n* junctions and charged interlayers (Vanzi, 1984; Pozzi, 1996), but have relied on the additional assumptions that the potential inside the foil is unaffected by the finite specimen thickness and that the results are independent of the relative permittivity of the foil. While these are valid for the much larger external fields present at *p–n* junctions, they are not appropriate for assessing the effect of a specimen surface on the phase contrast associated with variations in charge density that occur on a nm scale. We also assume that there are no variations in the magnitude of a dipole layer on the specimen surfaces close to the position of the layer (O'Keeffe & Spence, 1994), which would provide an additional contribution to the variation in potential. The present work will be extended in paper III to the fringing field surrounding a TEM foil containing a layer at which the change in potential is associated with differences in electron scattering factor.

† Image charge calculations are more commonly applied to high-energy electron diffraction in the different context of the self-image of an electron approaching a crystal (*e.g.* Tran Thoai & Zeitler, 1988).

2. Expressions for the electrostatic potential including fringing fields

As in paper I, we consider an interfacial charge density distribution $\rho(x) = \rho_b(x) - \rho_f(x)$, which is symmetrical about the centre of the layer at $x = 0$ (x is the direction normal to the interface plane) and is made up of a narrower 'bound' charge distribution $\rho_b(x)$ and a wider 'free' charge distribution $\rho_f(x)$. The layer is contained within an isotropic dielectric, which has thickness t in the incident-beam direction z and relative permittivity ε_r, and the total charge density $\int_{-\infty}^{+\infty}[\rho_b(x) - \rho_f(x)]\,dx$ is zero as a result of overall charge neutrality. Figs. 1(*a*) and (*b*) show the two image charge systems that are required to describe the contribution to the potential from one element of line charge per unit length λ inside and outside the slab, respectively. (The parameters that we refer to below when evaluating the potential at a point on the surface of the slab are also shown.) The image charges are located in a medium of relative permittivity ε_r, have magnitudes that are described using the coefficients α and β, and are obtained by reflecting each element of line charge per unit length, $\lambda(x', z') = \rho(x')\,dx'\,dz'$, making up $\rho(x)$ in the two specimen/vacuum interfaces, in turn. The boundary conditions at each of the two interfaces (*i.e.* continuity of the x component of the electric field E_x and the z component of the electric flux density $D_z = \varepsilon_0\varepsilon_r E_z$) are satisfied

through an appropriate choice of α and β, and the uniqueness theorem justifies the validity of the solution.* From Fig. 1, the contributions to $E_x(x_P, z_P)$ from a line charge $\lambda(x', z')$ are

$$(\lambda/2\pi\varepsilon_0\varepsilon_r)(x_P - x')(1 + \beta) \sum_{i=0}^{i=\infty} (\beta^i/r_i^2)$$

and

$$(\lambda/2\pi\varepsilon_0\varepsilon_r)(x_P - x')\alpha \sum_{i=0}^{i=\infty} (\beta^i/r_i^2)$$

inside and outside the slab, respectively, while the corresponding contributions to $E_z(x_P, z_P)$ are

$$(\lambda/2\pi\varepsilon_0\varepsilon_r)(1 - \beta) \sum_{i=0}^{i=\infty} \{\beta^i[r_i^2 - (x_P - x')^2]^{1/2}/r_i^2\}$$

and

$$(\lambda/2\pi\varepsilon_0\varepsilon_r)\alpha \sum_{i=0}^{i=\infty} \{\beta^i[r_i^2 - (x_P - x')^2]^{1/2}/r_i^2\}.$$

The boundary conditions are satisfied for all values of r_i when the coefficients α and β take values of

$$2\varepsilon_r/(\varepsilon_r + 1) \quad \text{and} \quad (\varepsilon_r - 1)/(\varepsilon_r + 1),$$

respectively. If the contributions to the potential from all real and image line charges λ_i at distances r_i are added

* While we have not been able to find it, it seems unlikely that this solution has not been published before; Finnis (1991) provides a similar solution describing the potential of a point charge between two conducting surfaces.

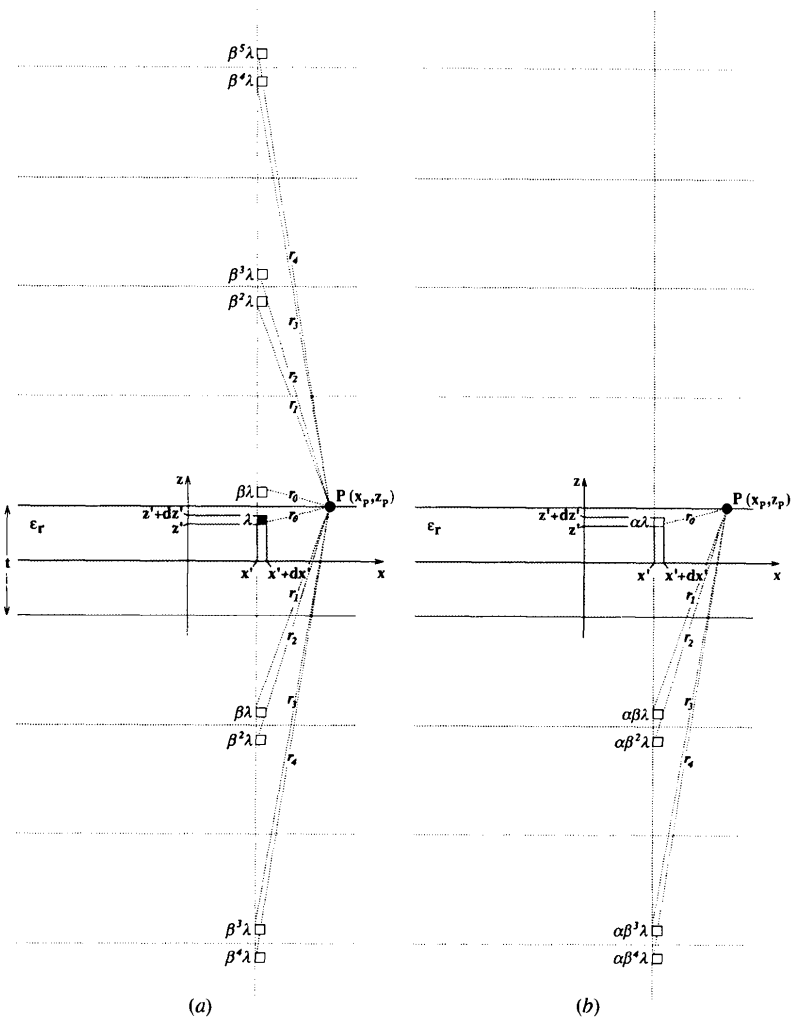

Fig. 1. Schematic diagrams showing the image charge systems that are required to describe the effects of surface polarization in a dielectric slab of permittivity ε_r and thickness t, which is surrounded by a vacuum and has embedded in it a single element of line charge $\lambda(x', z') = \rho(x')\,dx'\,dz'$ at position (x', z'). The image charge systems that are shown in (*a*) and (*b*) are used for determining the potential inside and outside the specimen, respectively. The parameters that are used to evaluate the potential at a point on the surface of the slab P are also shown.

together in the form

$$V(x,z) = (-1/2\pi\varepsilon_0\varepsilon_r)\sum_i \lambda_i \ln(r_i),$$

then the image charges shown in Fig. 1 result in the expressions

$$V_{\text{in}}(x,z) = (-1/2\pi\varepsilon_0\varepsilon_r)\int_{x'=-\infty}^{x'=\infty}\int_{z'=-t/2}^{z'=t/2}\sum_{i=-\infty}^{i=\infty}\rho(x') \times \Big(\beta^{|2i|}\ln[(x'-x)^2+(z'-z-2it)^2]^{1/2} + \beta^{|2i-1|}\ln\{(x'-x)^2 + [z'-z-(2i-1)t]^2\}^{1/2}\Big)\,dz'\,dx'$$

and

$$V_{\text{out}}(x,z) = (-\alpha/2\pi\varepsilon_0\varepsilon_r)\int_{x'=-\infty}^{x'=\infty}\int_{z'=-t/2}^{z'=t/2}\sum_{i=0}^{i=\infty}\rho(x') \times \Big(\beta^{|2i|}\ln[(x'-x)^2+(z'-z-2it)^2]^{1/2} + \beta^{|2i-1|}\ln\{(x'-x)^2 + [z'-z-(2i-1)t]^2\}^{1/2}\Big)\,dz'\,dx'$$

for the potentials inside and outside the specimen, respectively. These expressions for V_{in} and V_{out} can now be used to assess the effect of a finite specimen thickness on the phase contrast at a space charge layer. The inte-

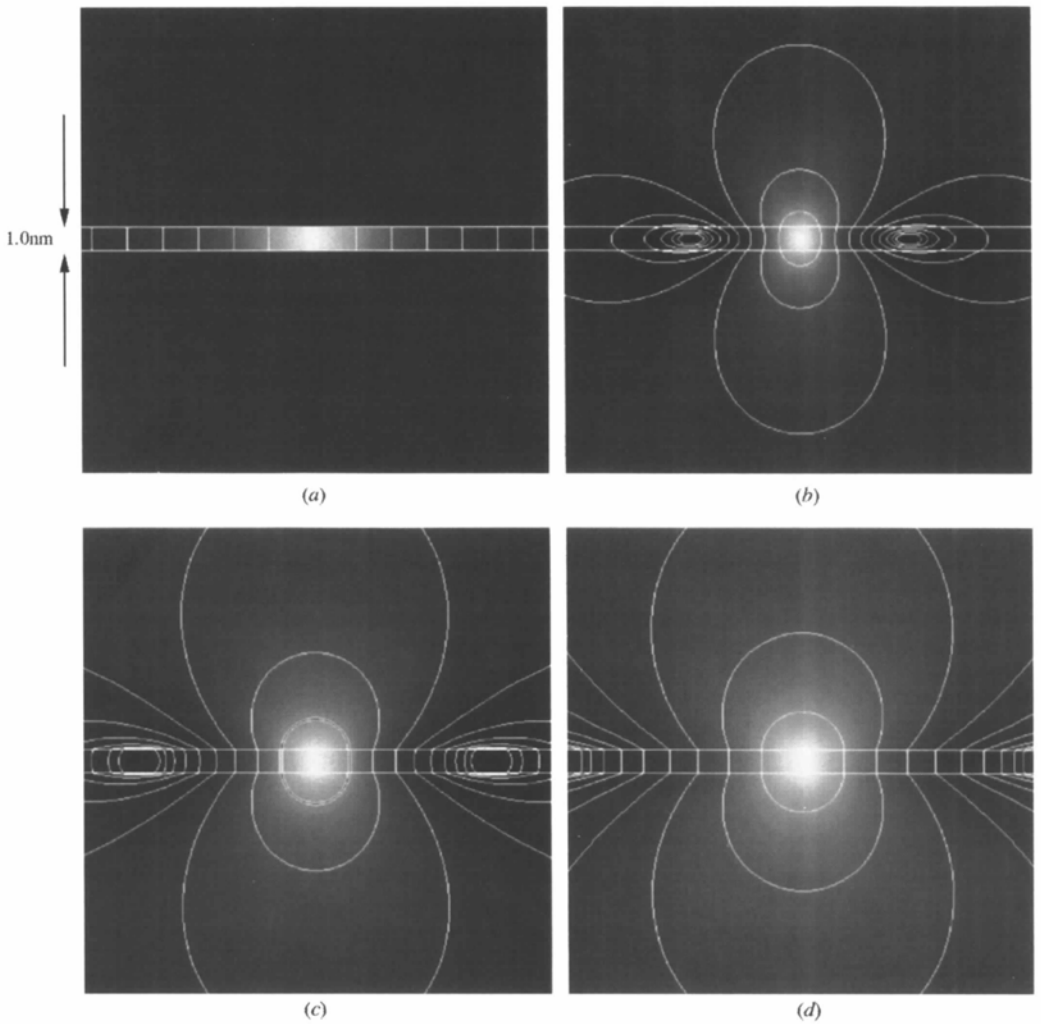

Fig. 2. Electrostatic potentials calculated for exponential space charge distributions $\rho_b(x)$ and $\rho_f(x)$, which have full widths at half-maximum of 0.5 and 3.0 nm, respectively, and projected charge-number densities of $\pm 10^{18}$ m^{-2} and are embedded in a dielectric slab of thickness 1 nm. (*a*) shows the form of the potential that would be calculated neglecting the effect of fringing fields, while (*b*), (*c*) and (*d*) show the results of full image charge calculations for dielectric slabs in which ε_r takes values of 1, 10 and 100, respectively. The horizontal lines show the positions of the specimen surface. Black and white correspond to the (different) minimum and maximum values of the potential in each picture, respectively, and the eight equipotentials shown are geometrically spaced, taking values of

$$\text{minimum} + (\text{maximum} - \text{minimum}) \times \{\tfrac{1}{2}, \tfrac{1}{4}, \tfrac{1}{8}, \tfrac{1}{16}, \tfrac{1}{32}, \tfrac{1}{64}, \tfrac{1}{128}, \tfrac{1}{256}, \tfrac{1}{512}\}.$$

gration with respect to z' can be performed analytically; the resulting expressions were used in the calculations reported below, but they are too lengthy to be worth reproducing here.

3. Results and discussion

Figs. 2–8 present calculations of V_{in} and V_{out} for charge-density distributions $\rho_b(x)$ and $\rho_f(x)$, which have full widths at half-maximum of 0.5 and 3.0 nm, respectively, total projected charge-number densities of $10^{18}\,m^{-2}$ (corresponding to approximately 10% of one atomic layer) and are exponential or Gaussian in form. These parameters correspond to representative values for space charge layers (see paper I for further details). V_{in} and V_{out} are shown directly in the form of contour plots in Figs. 2 and 3 for specimens of thickness 1 and 50 nm, respectively, for charge distributions $\rho_b(x)$ and $\rho_f(x)$, which are of exponential form, and with ε_r within the specimen taking values of 1, 10 and 100. (The 1 nm specimen thickness is an artificially small value and is included in order to illustrate the form of the potential as the extreme limit of a very thin specimen is approached.) The form of the potential at the space charge layer, which qualitatively resembles that of a quadrupole for a thin specimen, is clearly affected by both the specimen thickness and the relative permittivity of the material. The higher the value of ε_r, the less the potential *inside* the specimen is altered by the presence of the surfaces, but paradoxically the greater is the change in the potential *outside* the specimen. This can be seen more clearly in Figs. 4(*a*) and (*b*), which show the potential in the form of line profiles plotted along the incident-beam direction z (*i.e.* in the vertical direction in Figs. 2 and 3) for the 1 and 50 nm specimen thicknesses, respectively. These plots, which have all been scaled so that a value of unity corresponds to the potential within a specimen of infinite thickness, emphasize the larger effect of the

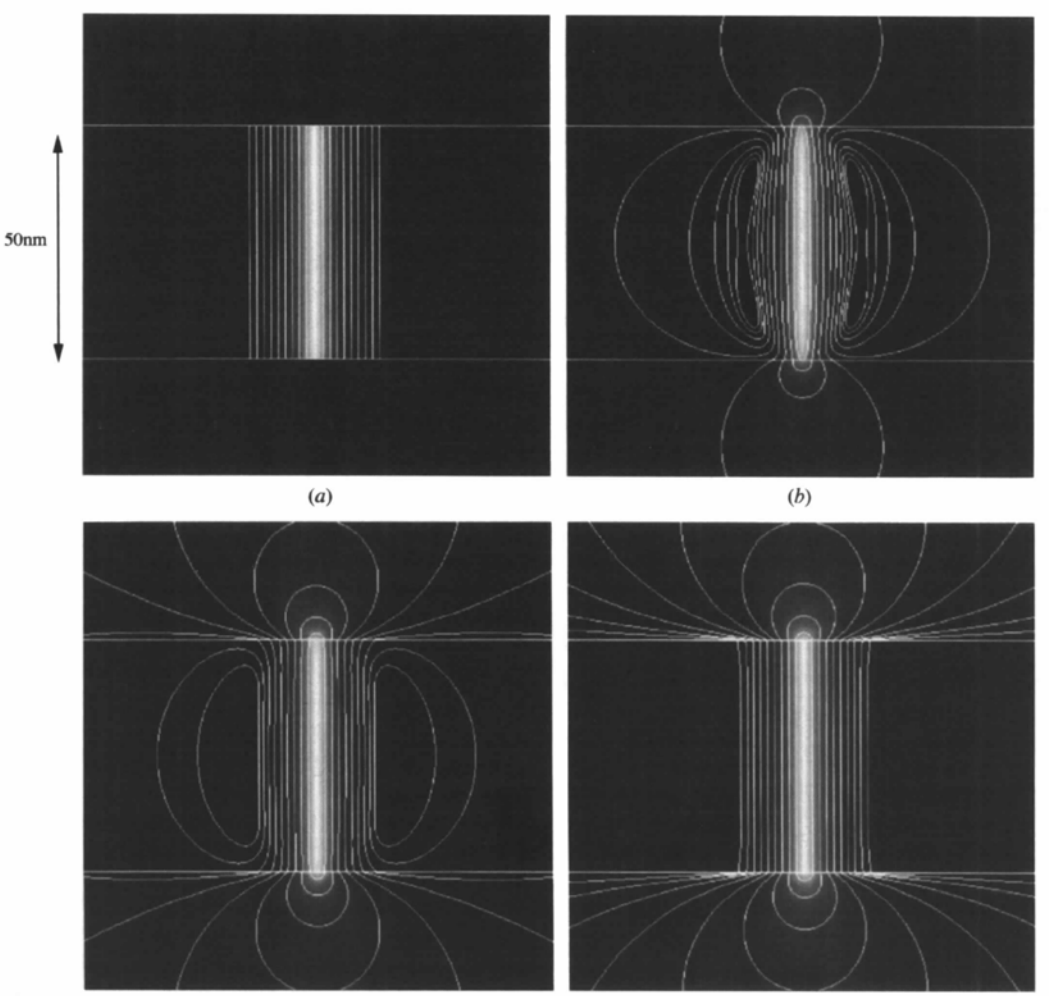

Fig. 3. As for Fig. 2 but for a specimen thickness of 50 nm.

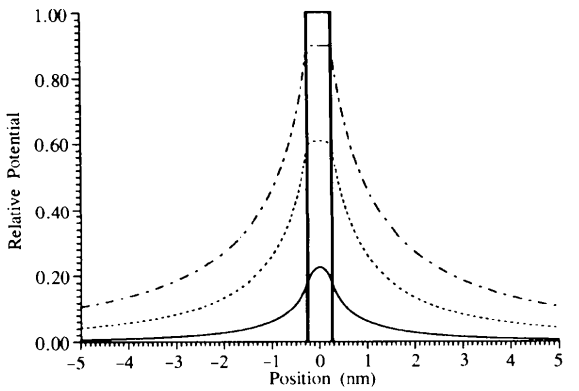

(*a*)

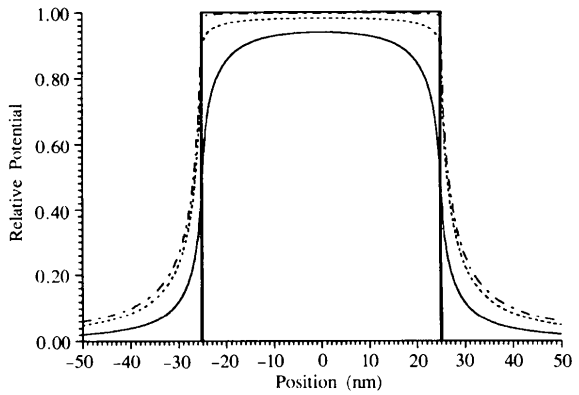

(*b*)

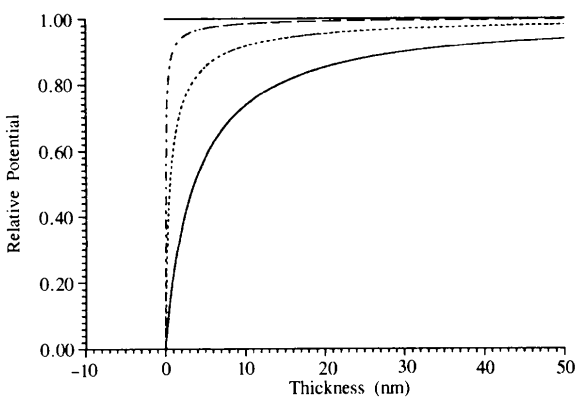

(*c*)

Fig. 4. (*a*) and (*b*) show line traces taken along the incident-beam direction z at position $x = 0$ for the images shown in Figs. 2 and 3, respectively (*i.e.* in the vertical direction in the middle of each image). (*c*) shows the corresponding value of the potential in the middle of the layer plotted as a function of the thickness of the dielectric slab. The images are all scaled so that the potential at the centre of the layer in a specimen of infinite thickness corresponds to a potential of unity. The profiles that would be calculated if the effects of fringing fields were neglected are shown as thick solid lines while those corresponding to full image charge solutions with ε_r taking values of 1, 10 and 100 are shown as thin solid, dotted and dot-dashed lines, respectively.

finite specimen thickness at lower specimen thicknesses for a given value of ε_r. Fig. 4(*c*) shows the magnitude of the potential at the centre of the dielectric slab, $V_{in}(0, 0)$, plotted as a function of specimen thickness for the exponential charge distributions that were used to obtain Figs. 4(*a*) and (*b*). All of the graphs tend to the potential expected for a specimen of infinite thickness, reaching a value of 90% of this at specimen thicknesses of 31, 8 and 1 nm for values of ε_r of 1, 10 and 100, respectively (*i.e.* the effect of fringing fields on the potential *within* the specimen is largest for the lowest value of ε_r).

While the fringing field surrounding a TEM foil has been shown in its entirety in Figs. 2–4, the form of the phase contrast visible at a charged layer is governed most directly by the total phase shift experienced by an electron as it passes through the specimen in the z direction, with respect to that of an electron passing through an identical region that does not contain a space charge layer. This total phase shift can be expressed in the form

$$\varphi(x) \approx k[(E + E_0)/E(E + 2E_0)] \times \left[\int_{|z|\le t/2} V_{in}(x, z)\,dz + \int_{|z|\ge t/2} V_{out}(x, z)\,dz\right],$$

where k is the wavevector, E the kinetic energy and E_0 the rest energy of the incident electron (*e.g.* Reimer, 1984). The contributions to $\varphi(x)$ from inside and outside the specimen are shown in Fig. 5 for charge distributions of exponential form for both of the specimen thicknesses examined above and for values of ε_r of 1, 10 and 100. The full widths at half-maximum of $\rho_b(x)$ and $\rho_f(x)$ are again 0.5 and 3.0 nm and the total projected charge-number densities are 10^{18} m^{-2}. It can be seen that at a specimen thickness of 1 nm the contribution to the phase shift from outside the specimen (which is broader than that from inside) always dominates both the magnitude and the form of the total phase shift. At the larger thickness of 50 nm, the majority of the phase shift now occurs inside the dielectric, the proportion from outside increasing with ε_r but always taking the form of a very slowly decaying background. Neglecting the fringing fields predicts the correct total phase shift when $\varepsilon_r = 1$ (*i.e.* for a charge distribution in free space). In that case, the juxtaposition of many thin layers and the superposition of their potentials would build up the same thick specimen with proportionately negligible fringing field regardless of whether the model in Fig. 2(*a*) or Fig. 2(*b*) was used – the projected potentials of the two models must therefore be identical. The effect of fringing fields on the phase shift is also consistent with the differences between the contour plots shown in Figs. 2 and 3. Fig. 6 shows equivalent graphs to those in Fig. 5, but now for Gaussian charge distributions. The effects of fringing fields are greater for exponential (Fig.

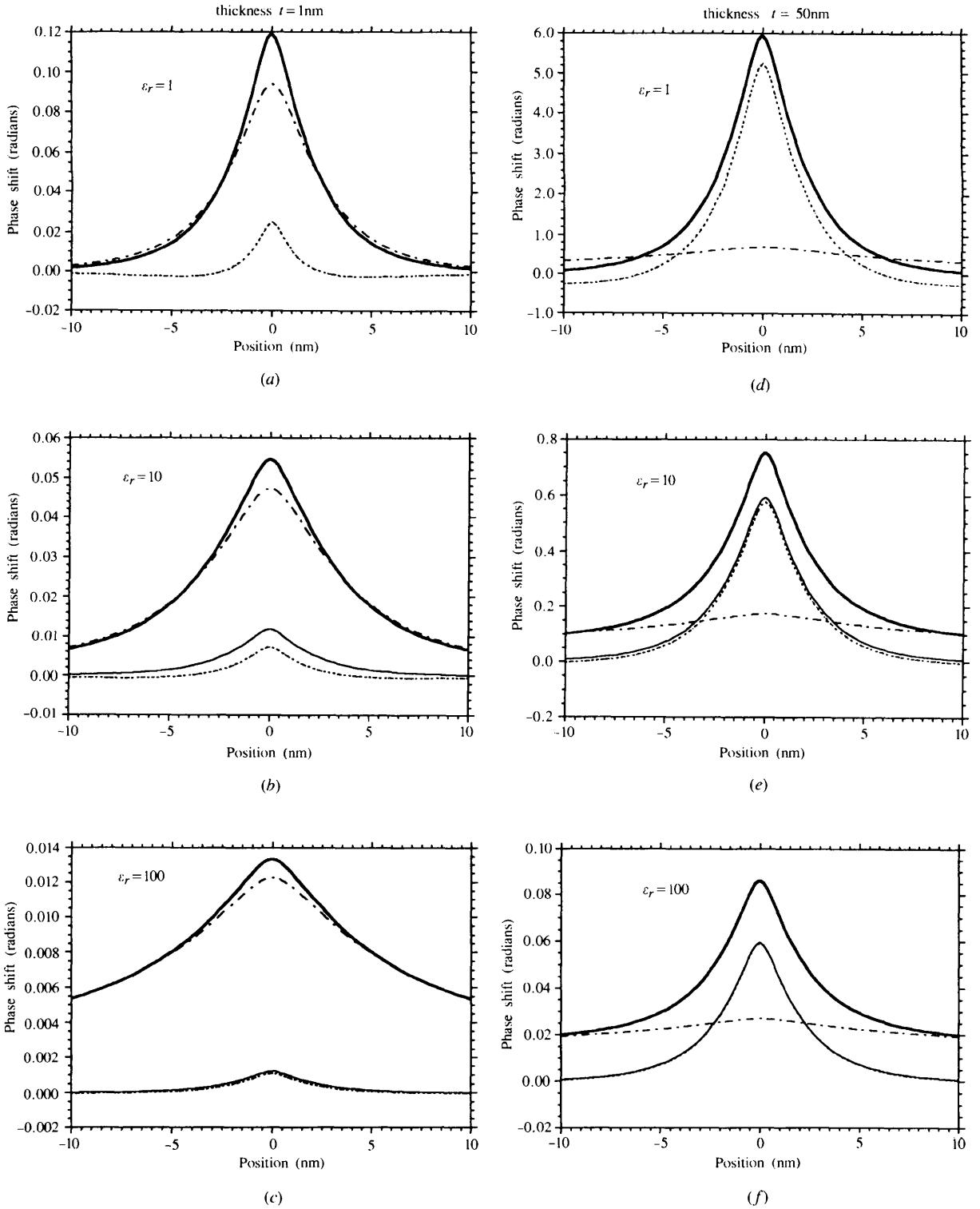

Fig. 5. The phase shift experienced by an electron as it passes through the specimen described in Figs. 2–4, with respect to that of an electron passing through an identical region that does not contain a space charge layer. (*a*)–(*c*) and (*d*)–(*f*) correspond to specimen thicknesses of 1 and 50 nm, respectively, with ε_r taking values of 1, 10 and 100 in sequence. The total phase shift that would be calculated if the effects of fringing fields were neglected is shown as a thin solid line (note different convention to Fig. 4), while the results of full image charge calculations for the total phase shift and the contributions to it from inside and outside the specimen are shown as thick solid, dotted and dot-dashed lines, respectively. [The thin solid and thick solid lines lie on top of each other in (*a*) and (*d*).]

5) than for Gaussian (Fig. 6) charge distributions that have identical full widths at half-maximum, presumably because the tail of the charge distribution extends further from the interface for the exponential model.

The fact that the form of a phase-contrast image need not be related *directly* to the magnitude of the total phase shift is illustrated by the Fresnel defocus images shown in Fig. 7, which have been calculated by applying a

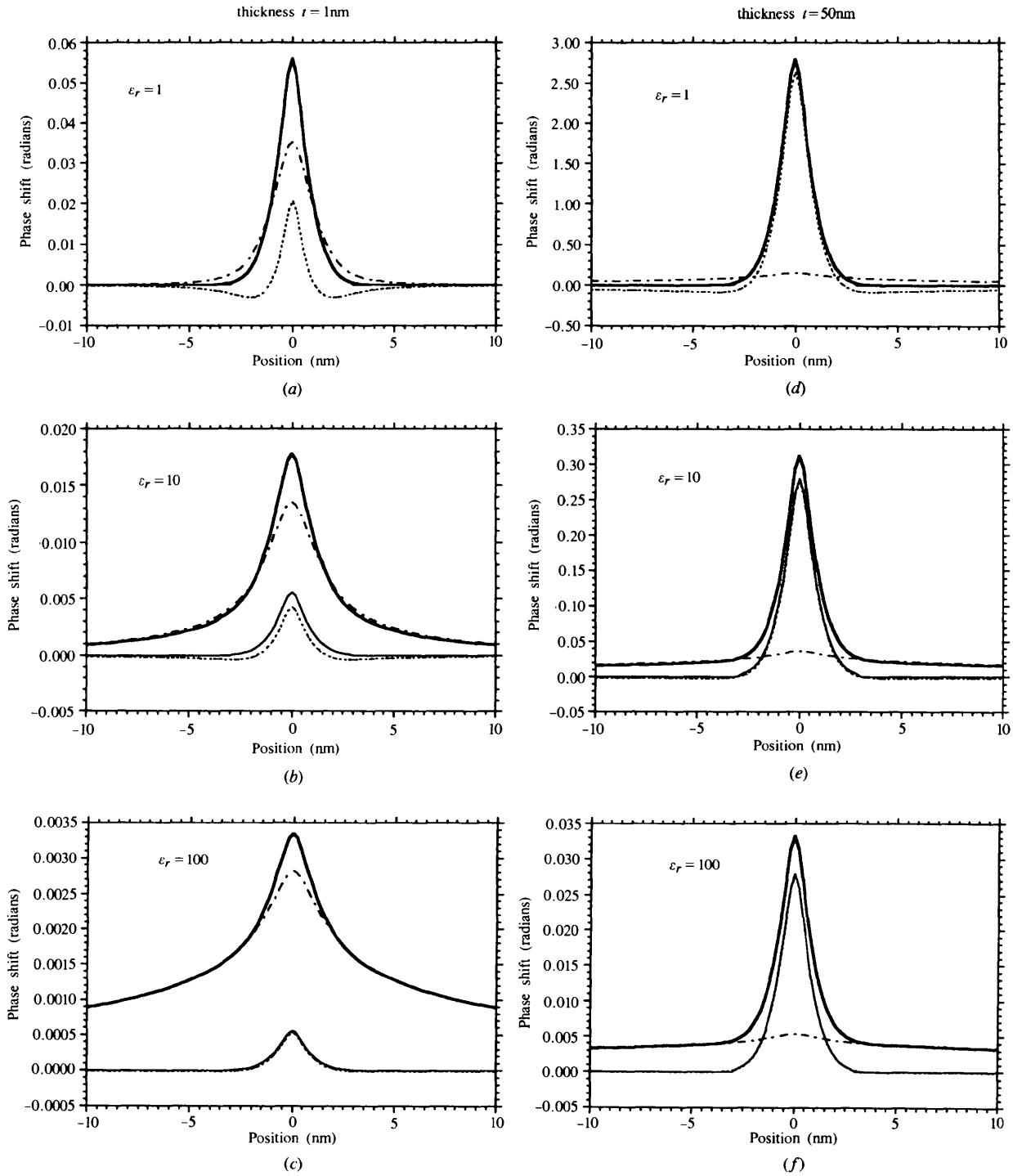

Fig. 6. As for Fig. 5 but now for Gaussian charge distributions $\rho_b(x)$ and $\rho_f(x)$, which have the same full widths at half-maximum of 0.5 and 3.0 nm, respectively, and projected charge-number densities of 10^{18} m^{-2}.

multislice algorithm* (see *e.g.* Ross & Stobbs, 1991) to successive horizontal slices of the images shown in Figs. 2 and 3 for an accelerating voltage of 200 kV, a beam semi-convergence angle of 0.5 mrad and a C_S of 2.8 mm. Both the magnitude and the spacing of the Fresnel fringes increase when fringing fields are included but, unlike the effects seen for the phase shift in Figs. 5–6, these changes are only significant for the lower specimen thickness. This is explained by the fact that at the higher thickness the contribution to the phase shift from outside the specimen is very broad (see Figs. 5 and 6) and Fresnel contrast is much more sensitive to local differences in the specimen potential than to its absolute value. At the lower specimen thickness, both the width and the charge density of a space charge layer would therefore be overestimated if experimental

* The phase-object approximation used by Pozzi (1996) is applicable for the larger defocus values used for Fresnel contrast images of *p–n* junctions, but would break down if applied at the imaging conditions considered here.

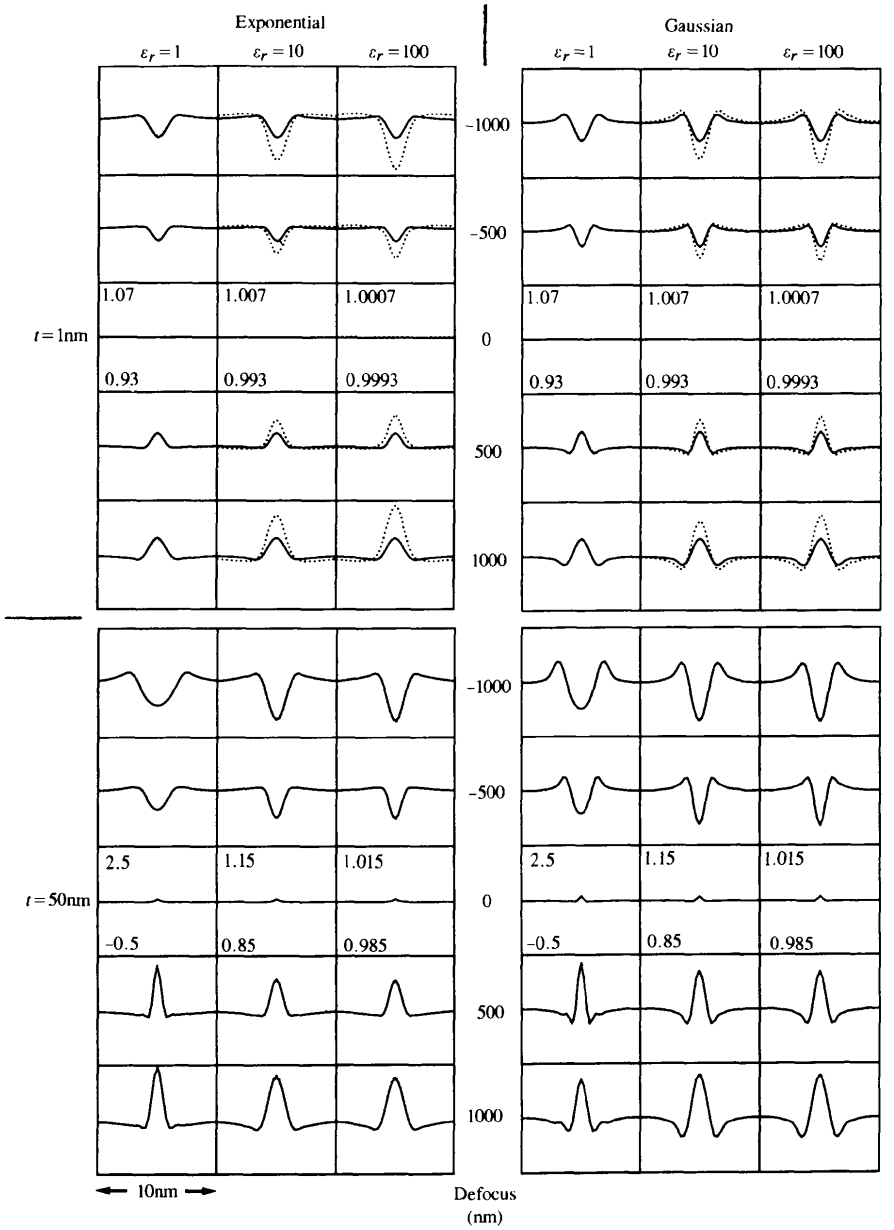

Fig. 7. Simulated through-focal series of images of both exponential and Gaussian charge distributions for dielectric slabs of thicknesses 1 and 50 nm and for relative permittivities of 1, 10 and 100. The simulations have been calculated by applying a multislice calculation to the images shown in Figs. 2 and 3 and correspond to an accelerating voltage of 200 kV, a beam semi-convergence angle of 0.5 mrad and a C_S of 2.8 mm. The solid and dotted lines correspond to simulations that neglect and include the effects of fringing fields, respectively.

data were compared with simulations that did not take fringing fields into account. (The examination of a higher thickness in order to avoid the effects of fringing fields would, however, increase the probability of the effective broadening of a layer that is not perfectly flat, as seen in projection.) Surprisingly, despite the large effect of the finite specimen thickness on both the potential (Figs. 2–4) and the phase shift (Figs. 5–6) at a space charge layer, the simulated Fresnel fringes in Fig. 8 show that the influence of fringing fields on Fresnel contrast is negligibly small above a specimen thickness of only 10 nm for the charge distributions considered here. The conclusion must therefore be that in most practical situations the simpler relations for determining the potential at symmetrical space charge layers such as those presented in paper I will be sufficiently accurate. However, this is not an indication that the effects of fringing fields are unimportant in other physical systems or especially when using other imaging methods such as electron holography.

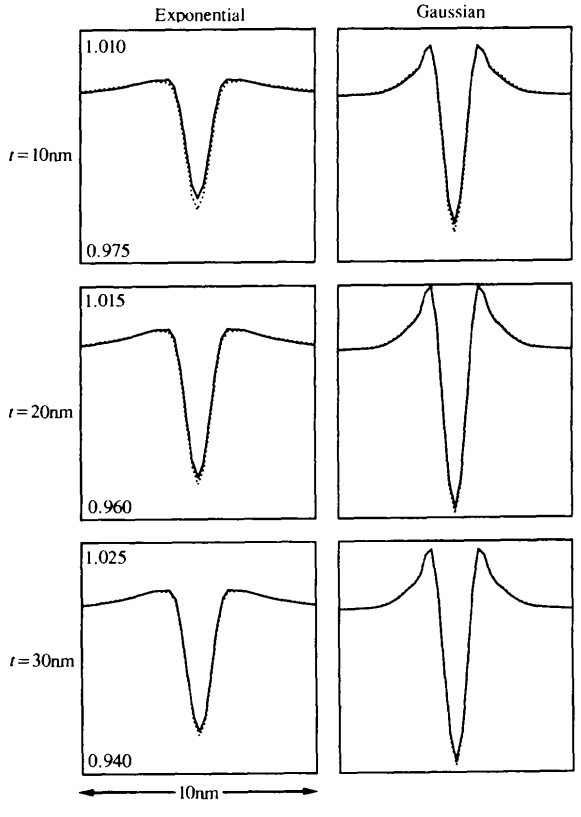

Fig. 8. As for Fig. 7 but for specimen thicknesses of 10, 20 and 30 nm, a relative permittivity of 10 and a single defocus value of 500 nm underfocus.

The results presented above are qualitatively similar to the work of Vanzi (1984) and Pozzi (1996), in that the contribution to the phase shift from outside the specimen has been predicted to be much broader than that from inside and contributes proportionately less to Fresnel contrast at all but the lowest specimen thicknesses. However, both Vanzi (1984) and Pozzi (1996) assumed in their calculations that the potential inside the specimen is unaffected by the presence of the free surfaces, which is clearly not valid for low specimen thicknesses and small values of ε_r (see Figs. 5 and 6). In addition, their calculations provide results that have no dependence on the value of ε_r within the material for a given potential distribution within the specimen, which is clearly *not* the case here.

4. Conclusions

Classical electrostatics theory has been used to determine the potential at a space charge layer that is contained within a dielectric slab of finite thickness. The form of the potential has been shown to be sensitive to both the thickness and the relative permittivity of the slab, with the contribution from outside the slab increasing with ε_r. At the lowest specimen thicknesses, both the width and the charge density of a space charge layer are overestimated if experimental Fresnel contrast data are compared with simulations that do not take fringing fields into account. The magnitude of the effects on Fresnel contrast reported is negligibly small above a specimen thickness of only 10 nm for the charge distributions considered here. It should be noted that this may not be the case for the fringing fields surrounding a TEM foil in a system such as a *p–n* junction or when using other imaging techniques such as electron holography.

We are grateful to the EPSRC (RED) and the Leverhulme Trust (WOS) for financial support.

References

Dunin-Borkowski, R. E., Saxton, W. O. & Stobbs, W. M. (1996). *Acta Cryst.* **A52**, 705–711.
Finnis, M. W. (1991). *Surf. Sci.* **241**, 61–72.
O'Keeffe, M. & Spence, J. C. H. (1994). *Acta Cryst.* **A50**, 33–45.
Pozzi, G. (1996). *J. Phys. D*, **29**, 1807–1811.
Reimer, L. (1984). *Transmission Electron Microscopy*, p. 57. Berlin: Springer-Verlag.
Ross, F. M. & Stobbs, W. M. (1991). *Philos. Mag.* **A63**, 37–70.
Tran Thoai, D. B. & Zeitler, E. (1988). *Phys. Status Solidi B*, **149**, 169–174.
Vanzi, M. (1984). *Optik (Stuttgart)*, **68**, 319–333.